Full Length Article

Rationally designed ultra-short pulsed laser patterning of zirconia-based ceramics tailored for the bone-implant interface

Norbert Ackerl [a],*, Alexander Hansen Bork [a], Roland Hauert [b], Eike Müller [c], Markus Rottmar [c]

[a] *ETH Zürich, Department of Mechanical and Process Engineering, Zürich, Switzerland*
[b] *Empa, Swiss Federal Laboratories for Materials Science and Technology, Joining Technologies & Corrosion, Dübendorf, Switzerland*
[c] *Empa, Swiss Federal Laboratories for Materials Science and Technology, Laboratory for Biointerfaces, St. Gallen, Switzerland*

A B S T R A C T

Ceramic composite materials are increasingly used in dental restoration procedures, but current ceramic surface designs do not yet achieve the osseointegration potential of state-of-the-art titanium implants. Rapid bone tissue integration of an implant is greatly dependent on its surface characteristics, but the material properties of ceramic composite materials interfere with classical surface modification techniques. Here, ultra-short pulsed laser machining, which offers a defined energy input mitigating a heat-affected zone, is explored for surface modification of ceramic composites. Inspired by surface textures of clinically relevant titanium implants, dual roughness surfaces are laser patterned. Raman mapping reveals a negligible effect of ultra-short pulsed laser ablation on material properties, but a laser-induced change in the wetting state is revealed by static contact angle measurements. Laser patterning of surfaces also influences blood coagulation, but not the attachment and spreading of osteoblastic cells. The presented laser machining approach thus allows the introduction of a rational surface design on ceramic composites, holding great promise for the manufacturing of ceramic implants.

1. Introduction

Since the development of dental restoration in the 1960s, the number of inserted implants increased every year. While initially the primary goal of a restoration with dental prosthetics was to gain full functionality, aesthetic aspects related to the color of implants and concerns over possible allergic reactions to metal implants have found increasing interest. To this end, advances in material science concerning novel alloys and engineered surface structuring have greatly contributed to enhanced implant performance [1,2]. Generally, the requirements for a biomaterial as tooth replacement are manifold: the mechanical properties have to match the application, the material should be cytocompatible, show no corrosion in physiological environments, should be highly wear resistant, and ultimately, it should provide rapid osseointegration [3]. Pure titanium and titanium alloys have been the standard materials for dental implants for decades [4], with their properties being well studied [5] and cost-effective production being well established. Importantly, titanium implants have proven long-term clinical survival rates [6]. Surface structuring is a well known approach to enhance osseointegration of implants and can be employed to achieve distinct surfaces at the body and neck to tailor hard and soft tissue interaction

[7–9]. The most suitable surface design is difficult to specify in detail due to the complex interplay of surface characteristics and biological processes taking place after implantation [10–12]. A commonly used routine treatment of titanium and its alloys is sandblasting followed by a wet-chemical etching step to generate a moderately rough surface, which is known to influence cell behaviour and ultimately to promote osseointegration [13]. To this end, it has been speculated that engineered surfaces with hierarchical elements in the micro- and nanometer range possibly enhance the biomaterial activity via controlling cell proliferation and differentiation [14]. Providing excellent control over process parameters, laser-induced surface structuring on titanium alloys utilizing short and ultra-short pulsed (USP) lasers has been explored [15–18]. A commercially available surface generated by laser structuring revealed a high potential by a micro-channel arrangement combined with nanostructures in preclinical studies [19,20]. However, introducing a defined hierarchical surface structure on metallic dental implants has yet to prove a significant advantage over state-of-the-art surfaces and is often accompanied by surface oxidation changing the chemical potential [21].

In recent years, metal-oxide ceramics and composites thereof have been proposed for several applications including dental and hip implants

---

[22]. Ceramics are especially promising materials for dental implants because of their high hardness, tunable toughness [23], and the ability to generate colors that more closely match the natural teeth. Furthermore, a lower risk for allergic reactions in comparison to titanium and metallic alloys has been reported for ceramics [4]. A large number of ceramics and composites are available, where the functionality can be specifically designed and tuned [24]. Especially, metal-oxide ceramics give the unique opportunity to design the mechanical properties [25], corrosion resistance [26], and wear behavior via alloying and adjusting the composition [27]. Today zirconia, alumina and alloys thereof with additives for stabilization of specific phases are the main ceramics used. However, these materials are hard-to-machine in the sintered state. The prevalent industrial manufacturing process for ceramic implants is grinding with diamond tools or machining in the green state before sintering [28] followed by an adapted sandblasting and etching step to generate a desired surface roughness. USP laser manufacturing is a promising technique to machine even ultra-hard materials pointing to a minimal heat-affected zone, no wear, and high geometric flexibility. This technology has shown high applicability to alter the wettability [29,30], tribological performance [31], and reaction paths in electrocatalysis [32]. Recently, a rapid-prototyping approach using USP lasers to manufacture complex 3D alumina-toughened zirconia (ATZ) dental implants with controllable roughness and high precision was presented [33]. However, the use of laser manufacturing for dental implants is still an emerging field, wherein its potential impact on ceramics has still to be unraveled. To date, little has been investigated on USP laser ablation of technical ceramics, with the choice of laser source and strategy still being under discussion [34,35] and the research is largely focused on cutting and drilling processes [36,37]. Studies concerning the impact of USP laser marking on hydro-thermal aging of ATZ and zirconia-toughened alumina (ZTA) pointed to a negligible influence of orthogonal laser ablation [38]. Recently, the applicability of defined surface patterns on complex ATZ ceramic implants was demonstrated [39] and a femtosecond pulsed laser patterning of ATZ was reported [40]. However, the influence of these surface patterns on cell responses was not explored.

In this study, rationally designed hierarchical structures inspired by state-of-the-art implant surfaces are introduced on ATZ and tetragonal zirconia polycrystal (TZP) ceramics by USP laser machining. A systematic ablation study presents the characteristics allowing well-defined and reproducible laser machining and the introduced micro- and nanostructures are assessed in vitro for their influence on blood coagulation and cell adhesion, which represent the early steps of implant integration. Following, the surface state is analyzed and conclusions are drawn on the impact of chemistry and laser-induced surface potential changes on the observed bio-response.

2. Material and experimental routines

2.1. Zirconia composite characteristics

Ceramic materials are potential candidates for dental implants, for which increasing the fracture toughness is one of the main challenges. The most important systems are metal-oxide based ceramics like alumina-toughened zirconia (ATZ), zirconia-toughened alumina (ZTA), partial stabilized zirconia (PSZ) and tetragonal zirconia poly-crystal (TZP). Yttria stabilizes the cubic or tetragonal zirconia phase depending on stoichiometry and rectifies the corrosion resistance in aqueous environments, thereby being an ideal candidate to tailor the materials characteristics for dental restoration [22]. These ceramics exhibit an indirect wide-band gap depending on the material and phase, where ZrO_2 is monoclinic at room temperature with two transitions to a tetragonal and cubic phase in the high-temperature regimes. The gap in the tetragonal phase is about 5.5 eV [41,42] and therefore non-linear absorption at high power density enabled by USP laser ablation is necessary for material removal. Alumina has a gap of about 8.7 eV in the

α-phase existent in ATZ for toughening and TZP as by-product [43,44]. Therefore, pure alumina in the α-phase is studied to compare the laser ablation characteristics to zirconia investigating a possible influence between ATZ and TZP. These gaps play a role in the electron generation and influence the ablation behavior and following threshold fluence. All specimens are supplied by Metoxit AG Switzerland in the used geometry and a mean roughness $R_a < 200$ nm. Generally, HfO_2 up to 2 wt% present in the ceramic as contaminant. The ATZ composition in weight percentage is 76%ZrO_2, 20%Al_2O_3, 4%Y_2O_3 and TZP is constituted by 94% ZrO_2, 5%Y_2O_3, and 0.25%Al_2O_3 with a mean grain size of 0.4 µm and 0.35 µm accordingly. The alumina specimen is of a 99.8% purity with a mean grain size of 5 µm.

2.2. In vitro assessment

Blood coagulation and the attachment of osteoblast progenitor cells is assessed as reported previously [12], with an schematic overview being provided in Fig. 1. In brief, all samples have been cleaned ultrasonically in pure ethanol and sterilized at 160 °C dry heat for 2 h. Human whole blood gathered by a standard venipuncture technique is used and partially heparinized. The specimens are placed in a round-shaped polytetrafluoroethylene holder and each chamber is filled with fresh blood, closed and placed on an orbital shaker for 13–15 min to allow for blood coagulation. Subsequently, the blood on the samples is removed before rinsing them with pre-warmed phosphate-buffered saline (PBS). Primary human bone progenitor cells (HBC) from different donors are used to study cell adhesion and proliferation as well as osteogenic differentiation on the blood pre-incubated surfaces. HBC attachment and spreading is assessed by confocal laser scanning microscopy (CLSM) of the samples after 24 h of culture. The samples are then rinsed with PBS, fixed, and stained for the actin cytoskeleton with AlexaFluor 488-conjugated phalloidin and nuclei with DAPI for 1 h at room temperature. Fibrinogen is labelled by incubation with a monoclonal anti-human fibrinogen antibody followed by incubation with the corresponding anti-mouse Alexa Fluor 555 antibody for 1 h each. The samples are subsequently evaluated with a CLSM (LSM780, Carl Zeiss).

2.3. Laser machining configuration

The principal configuration of the used laser setup is depicted in Fig. 2. An USP laser source Amphos 200 in a master oscillator pulse amplification configuration realized by Innoslab technology with a second harmonic unit emits highly intense sub 1 ps 515 nm pulses with a maximal pulse energy of 300 µJ. High-precision X, Y, and Z mechanical axes (ANT180, PRO165) from Aerotech allow a distinct positioning of the specimen and adjusting of the focus of the 163 mm telecentric f-theta lens. Using a telescope with threefold magnification and divergence compensation enables a focal spot diameter of about 11 µm, where wave plates set the circular polarization state in the focal plane for defined ablation. A galvo scanhead (Scanlab Hurryscan II) enables a fast beam steering and the complete configuration is controlled by Aerotech drives and the A3200 software for synchronous axes movement. The laser machining utilizes a 2.5D strategy, where the surface design is generated using CAD tools and a developed CAM software for the laser hatch and path computations [45]. This configuration allows a straightforward laser machining of distinct structures with high geometric flexibility.

2.4. Analysis routines

The laser machined samples are inspected by light microscopy and measured by confocal microscopy (Leica DCM3) using a 50x objective lens with a stitching routine. Scanning electron microscope (SEM) studies (Hitachi SU-70) allow to resolve the micro- and nanostructures with high resolution. Raman spectroscopy (Thermo Scientific DXR2) at 455 nm excitation wavelength and a penetration depth of a few hundred
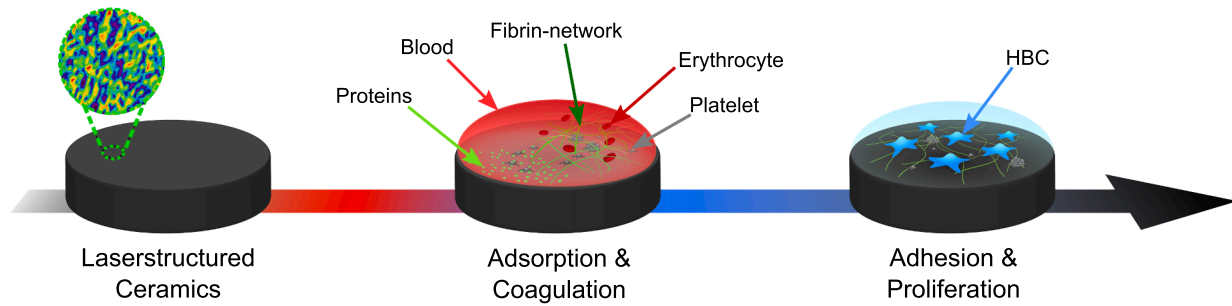
Fig. 1. Routine for the biological assessment, where the laser-structured ceramic surface is first tested for blood coagulation characteristics after 13–15 min followed by studying the adhesion and proliferation of HBC after 24 h, adapted from [12].
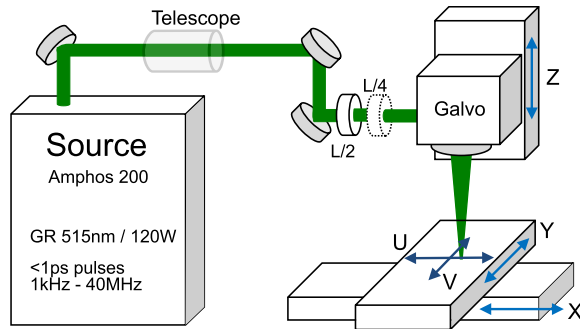

Fig. 2. Experimental laser test bed constituted by a source, beam guidance, optical (U, V), and mechanical (X, Y, Z) axes for fast beam steering plus positioning.

nanometers identifies the crystalline phase of the ceramic and X-ray photon emission spectroscopy (XPS) assesses the quantitative surface-near chemical constituents. A PHI Quantum 2000 spectrometer (Physical Electronics) using a spherical capacitor energy analyzer with Al$K\alpha$ radiation at 1486.68 eV working at a vacuum of $5 \cdot 10^{-7}$ Pa enables an automated measurement routine. Following, the assessment of all samples under investigation runs in one measurement cycle with the XPS calibrated at the gold 4f line at (84.0 ± 0.1) eV.

3. Results and discussion

3.1. Laser ablation characteristics of ATZ and TZP

To generate defined microstructures 2.5D ablation is utilized and the material removal rate (MRR) is attained by machining pockets. A total of 45 layers of the respective material are removed using a hatching distance of 5 μm and 23° rotation of each subsequent layer reducing the accumulation of deviations. The fluence regime is kept below 1.4 J cm^{-2} and Fig. 3 presents the scaled specific MRR. Assuming the laser pulses to be Gaussian in space and time allows to identify the threshold F_{th} and optimal F_{opt} fluence values. If the MRR is divided by the used average power P_{avg}, the specific MRR describing the ablation efficiency can be determined [46]. Keeping the ablation strategy and size of the pockets unchanged reduces the dependency from a volume removal rate to the ablation depth z_{abl} or layer thickness z_{layer}. Fig. 3 graphs the modified specific MRR following the functionality

$$z_{abl}/P_{avg} \propto \frac{\delta_{opt}}{F}\ln^2\left(\frac{F}{F_{th}}\right) \tag{1}$$

being proportional to the optical penetration depth δ_{opt}, fluence F, and threshold fluence F_{th}. A least-square fitting allows to identify the threshold and optimal fluence from the experimental study presented in Fig. 3. Hence, the functionality allows to estimate the multi-pulse F_{th} by
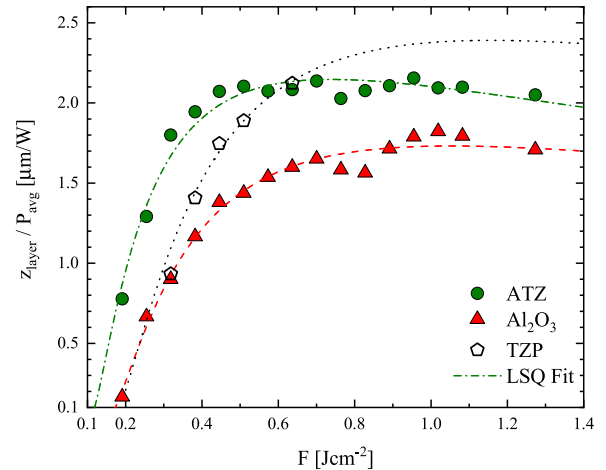

Fig. 3. Specific material removal rate given by the ablation layer depth z_{layer} scaled by the average power P_{avg}. To determine the multi-pulse threshold and optimal efficient fluence a least square curve fitting following (1) and (2) is applied.

extrapolation to zero layer thickness and assuming a full incubation reaching the saturation regime [47,48]. Setting the derivation of (1) to zero leads to a proposed optimal fluence for highest power efficiency of ablation to

$$F_{opt} \approx e^2 F_{th}. \tag{2}$$

Here, the optimal fluence depends solely on F_{th} and inherently the focal beam radius w_0. Keeping the pocket-size and laser strategy unchanged leads to the same processing time for all experiments [49,50]. The attained multi-pulse threshold of ablation from fitting and extrapolation to Eq. (1) for sub-picosecond pulsed ablation reveals 0.13 J cm^{-2} for ATZ, 0.18 J cm^{-2} for alumina, and 0.21 J cm^{-2} in case of TZP. Moreover, the maximum at the optimal fluence is found at 0.9 J cm^{-2} for ATZ, 1.3 J cm^{-2} for alumina, and 1.56 J cm^{-2} for TZP respectively. Generally, the proposed trend for the ablation characteristic is followed by the experimental data allowing to estimate the anticipated optimal and threshold fluence. Hence, the power density necessary for excitation defines a small parameter window near the threshold value enabling a defined microstructuring by multi-photon absorption without crack initiation. In addition to the microstructures, a second hierarchical roughness is generated as depicted in Fig. 4, tailored for an enhanced osseointegration. To study the evolution of ablation focusing on nano-roughness, the laser repetition rate is set to 10 kHz and the pulse-to-pulse overlap altered by adjusting the galvo scan speed leading to separate ablation events up to high overlap. This parameter study leads to the ablation behavior of the ceramics, where a comparable surface has to be introduced to both materials. A sharp onset of ablation is observed, which is
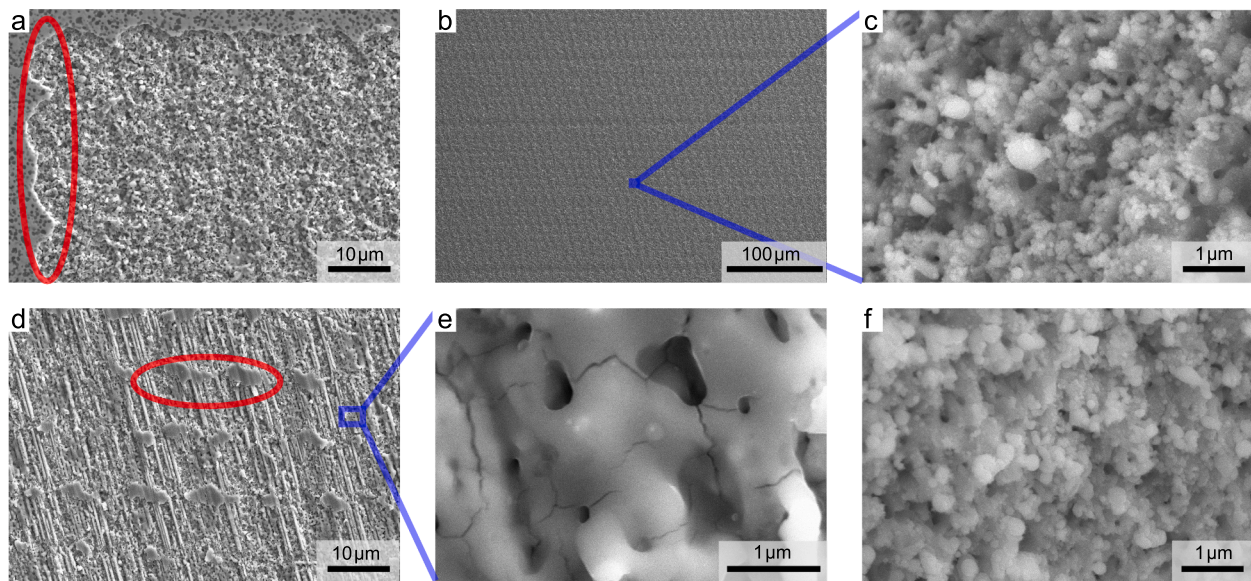
Fig. 4. SEM micrographs presenting the surface structure of the laser machined ATZ (a-c) and TZP (c-f) specimen. The pulse and hatch distance is optimized (a) leading to a homogeneous nano-roughness (b). A defined ablation is a necessity mitigating cracks (e) and generating a comparable surface on both substrates in the magnified graphs presented in (c) and (f).

in contrast to metals, where up to the threshold no obvious modification of the surface is observed followed by a layer thickness of about 1 μm in agreement with literature [51]. Clearly, the ablation characteristics are governed by non-linear effects and multi photon absorption processes for these wide-band gap materials [52]. Fig. 4 presents the approach for achieving a nano-roughness, where the minimum pulse-to-pulse and hatch distance is attained for ATZ in the upper row (a-c) and TZP at the bottom (d-f) shown at different laser parameters summing up a broader assessment. The aim is reaching a reproducible roughness in short processing time, where the pulse-to-pulse overlap and hatching distance is varied in the range between 1 μm to 10 μm. Fig. 4a presents the distance set to 10 μm, where the single ablation events can be observed (at the rim marked with the red ellipse). Setting the distance to 4 μm leads to a roughness comparable to the one achieved by 2.5D ablation with multiple layers presented in Fig.4b. Ceramics are in principle brittle and thermal gradients or local melting can lead to cracking if the local energy input is too high [53]. Therefore, the maximal MRR is limited by the usable fluence, where Fig. 4e corroborates this assumption revealing small cracks at a fluence of only 1.3 J cm^{-2} below the found optimum for multi-pulse ablation, where parts of the surface shown in Fig. 4d are not completely ablated. After this qualitative study on surface roughness by altering the laser parameters between near the threshold fluence up to the optimum and adjusting the pulse and hatch overlap, a fluence of 0.5 J cm^{-2} for ATZ and 0.7 J cm^{-2} for TZP is identified. The laser-induced nano-roughness on both specimens is comparable, as depicted in the magnified graph of Fig. 4c and Fig. 4f. It is anticipated, that the coupling of the laser light starts at the grain boundaries and testing the same set of parameters near the threshold fluence reveals an inhomogeneous ablation state, where only parts of the pocket are ablated. The origin might be the slightly different ablation threshold observed between the alumina, ATZ and TZP ceramic, where the threshold of the additional alumina particles is in between the two compounds, while additionally introducing more grain boundaries compared to the TZP with the zirconia matrix.

3.2. Rational surface design and laser machining

In this study, textured surfaces inspired by successful implant designs reported in literature [54,55] are designed and generated by laser machining. Considering the knowledge of osseointegration with

titanium implants in contact with human osteoblastic cells points to a random structure with hills and grooves of a pitch with about 50 μm and peak-to-valley height of approximately 30 μm [8]. Additionally, a second hierarchical morphology in the sub-micrometer range was suggested to enhance implant-tissue interactions [24]. In order to assess the impact of the structuring on the initial steps of implant integration, three groups of surfaces from each material are studied. An unprocessed surface (blank), rough surface (nano), and a combination of random microstructures with the same roughness (micro&nano) are explored. A pseudo-randomly designed 3D structure was generated by using a random number generator and scaling the height between ±15 μm keeping the pitch at 50 μm with a measurement of the surface presented in Fig. 5a. For the laser manufacturing the Amphos 200 SHG radiation at 515 nm wavelength with sub-picosecond pulses at a repetition rate of 200 kHz, average power of 0.45 W for ATZ and 0.55 W for TZP, a focal beam diameter of 11 μm, beam distance l$_b$ = 5 μm, and scan speed of 300 mm s^{-1} was used. With this set of parameters, 12 layers were ablated to reach the premeditated depth and each adjacent layer was rotated by 29° mitigating the accumulation of geometrical errors.

The nano surfaces are generated with a different set of laser parameters in a two-step pass with a second orthogonal hatched layered ablation step shown in Fig. 5b. The average power was altered to 0.2 W for ATZ and 0.3 W for TZP with a reduced repetition rate of 10 kHz to diminish the influence between the adjacent pulses. The beam distance was set to 4 μm with a scan speed of 200 mm s^{-1} leading to a processing time of below 1 min per sample. The micro&nano hierarchical surfaces are manufactured within 7 min on the disc-shaped specimen with an area of 20 mm^2 and the central region thereof in Fig. 5a is comparable for both ceramic substrates. A qualitative SEM assessment reveals the surface topography of the laser generated surfaces in more detail focusing on the micro&nano structure in Fig. 6. The magnified micrographs reveal the hierarchical roughness, where microstructures constitute the peak-valley morphology, while featuring a nano-scale roughness similar to the designed roughness shown in Fig. 4, thereby staying true to the laser parameter optimization. The black appearing alumina particles shown in Fig. 4a are contained and Raman measurements are carried out to determine possible phase changes.

Stabilized zirconia ceramics can undergo a phase transition from tetragonal to monoclinic upon heating, leading to a volume increase and stressed surface or even to the development of cracks [33,53]. There,
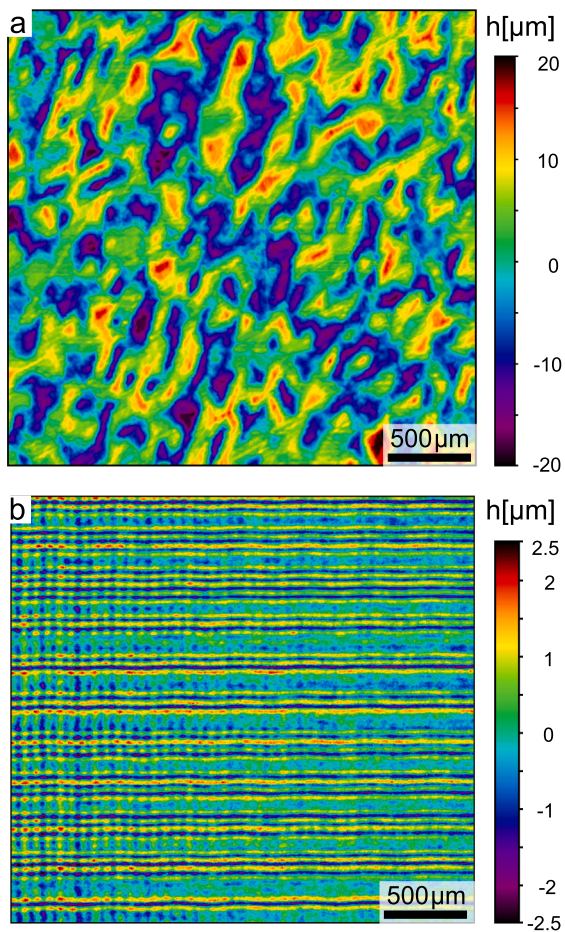
Fig. 5. Surface design and confocal measurement of the ATZ ceramic. (a) The superposition with microstructures and random height with spacing of 50 μm and a peak to valley height below 40 μm. (b) Nano surfaces are laser-structured by cross-hatching and 4 μm distance.

confocal Raman mapping is utilized to measure a map of an area spanning 400 mm^2 attaining 100 spectra of the blank and laser patterned nano surfaces. This allows a sound statement on the phases and the representative measurements are presented in Fig. 7 for ATZ (a) and TZP (b) samples. For both samples, viz. ATZ and TZP, the spectra reveal a good signal-to-noise ratio and the four characteristic peaks (T1 - T4) for the tetragonal configuration are located at the expected positions as reported in literature [56]. Indeed, the measurements confirm the tetragonal phase of both ATZ blank and nano (7a). In some spots of the blank sample, an impurity monoclinic phase is observed by the double peak structure centered at 180 cm^{-1} and the small peak at 378 cm^{-1}. Interestingly, the amount of the monoclinic phase is reduced for the ATZ specimen after laser patterning, which is in agreement with literature comparing ceramic implants subjected to different manufacturing techniques [33]. Therefore, USP laser machining can be used with a distinct set of laser parameters allowing a defined patterning of both ceramic specimens. Moreover, there is no observable shift in the peak positions apparent, which points to an unstressed state that underlines the negligible impact of USP laser machining on the material.

Structuring the TZP with the adapted laser parameters allows machining comparable nano and micro&nano structures, where a comparison of statistical roughness measurements is given in Table 1. Assessing a set of surface and profile roughness measures, the small structures presented in Fig. 6 are not adequately covered by the confocal measurement. This nano-roughness is crucial for the wetting behavior and subsequent bio-response, and is assessed by a qualitative SEM study. For the analysis of the confocal area measurements, five parallel line profiles and additionally the statistical surface moments root mean square height S_q, arithmetical mean height S_a, and maximum height S_z are used measuring two surfaces per manufactured batch. Using a proposed cut-off $\lambda_c = 80$ μm from ISO standard 4288-1996 and an evaluation length longer 0.4 mm allows to decouple roughness and waviness of the surface. The values presented in Table 1 prove a high reproducibility of the laser generated surfaces on both ceramics rounded to 100 nm respecting the precision of the optical measurement.

3.3. Blood- and cell-material interaction

Blood material interaction of the laser-structured specimens is assessed by SEM analysis in Fig. 8. Attachment and activation of
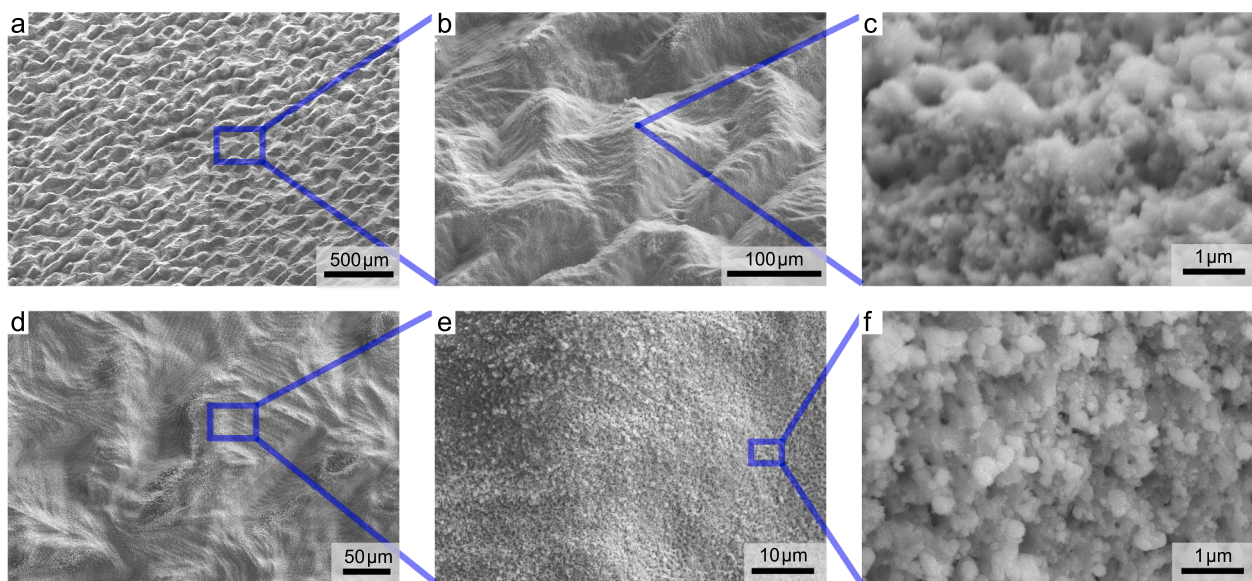

Fig. 6. SEM graphs of the micro&nano hierarchical structures on ATZ (a-c) in the upper row tilted by 40° and TZP (d-f) at the bottom. The rationally designed micro features (a,b,d,e) are superimposed by the designed nano-roughness (c,f). The quality of the structures on both materials is comparable as shown with higher magnification in (c) and (f).
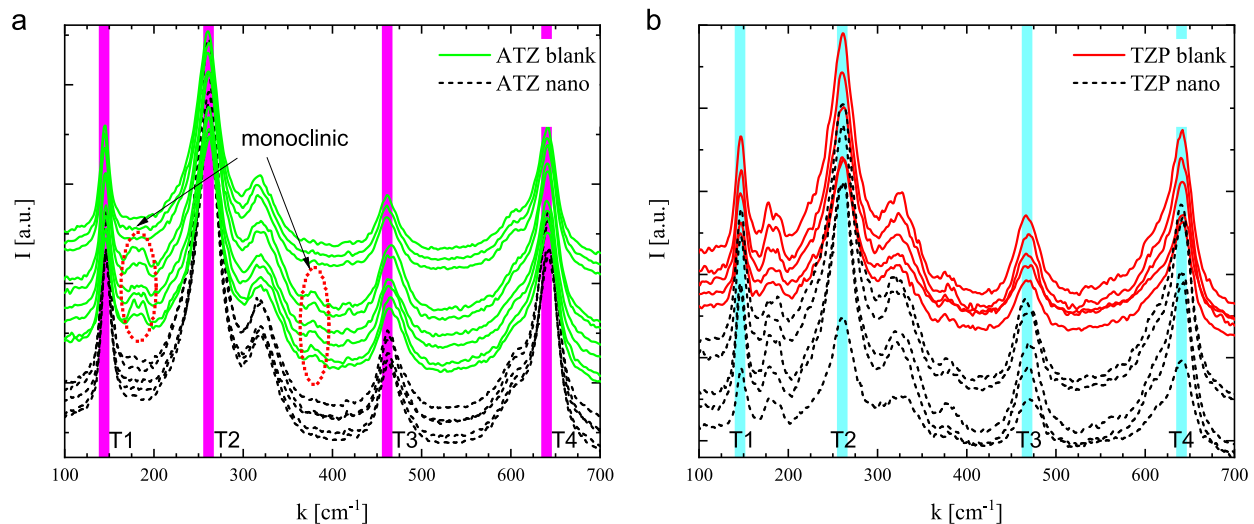
Fig. 7. Raman measurements of the blank, nano ATZ (a) and TZP (b) composite revealing the persistence of the tetragonal phase with an offset for clarity. The spectra for the blank (solid) and nano (dashed) surfaces point to a negligible impact of USP ablation reducing the monoclinic phase for ATZ.

Table 1
Statistical roughness moments from confocal measurements of the surfaces presented in Fig. 5. Nine samples per material are laser machined in one batch (No.) and analyzed, leading to mean and standard deviation of $S_{q,a,p}$ and $R_{q,a,z}$.

Sample	No.	S_q [µm]	S_a [µm]	S_p [µm]	$R_{q,RMS}$ [nm]	R_a [nm]	R_z [µm]
ATZ nano	1	1.6 ± 0.1	1.3 ± 0.1	4.8 ± 0.7	600 ± 35	475 ± 30	2.9 ± 0.3
	2	1.5 ± 0.2	1.2 ± 0.1	5.1 ± 0.9	615 ± 25	490 ± 25	2.5 ± 0.2
TZP nano	1	1.9 ± 0.6	1.4 ± 0.5	4.9 ± 0.8	595 ± 15	480 ± 10	2.8 ± 0.1
	2	1.6 ± 0.4	1 ± 0.2	4.4 ± 0.6	590 ± 15	475 ± 15	2.9 ± 0.2
ATZ micro&nano	1	7 ± 0.3	5.8 ± 0.2	21 ± 1.4	–	–	–
	2	6.9 ± 0.3	5.7 ± 0.2	19.5 ± 1.9	–	–	–
TZP micro&nano	1	6.6 ± 0.2	5.4 ± 0.2	17.5 ± 1.4	–	–	–
	2	6.7 ± 0.2	5.5 ± 0.3	18.6 ± 1.2	–	–	–

platelets as well as fibrin network formation could be observed, with blank surfaces showing the highest degree of coagulation. Compared to blank, nano as well as micro&nano surfaces show a greatly reduced blood coagulation where fibrin network formation has not yet started. However, blood coagulation serves only as a first assessment and the surface coverage with blood components and a fibrin network strongly depends on the incubation time. In order to investigate the influence of laser-induced surface structures on cell attachment, primary HBC seeded on blood pre-incubated samples are studied by confocal laser scanning microscopy after 24 h, presented in the bottom graphs of Fig. 8a-f. Generally, the cells show good attachment and spreading on all surfaces. While no difference in cell attachment and spreading could be observed between the different surfaces, the cells showed a preferential alignment along the groove structure on the nano surfaces that originate from laser processing with the hatch distance l_b most prominently observed in Fig. 8e. While the observed impact of the designed surface structures on cell adhesion is small after 24 h, future studies on cell proliferation and differentiation over longer time periods should reveal surface-dependent changes in cell behavior.

3.4. Surface chemistry and state

The first blood contact is greatly influenced by the wetting characteristics at the surface altering the rate of coagulation, which depends on surface chemistry and topography [57]. Measuring the contact angle therefore allows a first assessment of the surface state. A Wenzel state is expected to act as a surface state amplifier. Hence, a hydrophilic behavior will reveal a reduced CA and vice versa a hydrophobic one an

increased CA by laser patterning. Fig. 9 presents the attained CA of the specimen, where at least two samples with more than three independent measurements are considered. After dispersing a 1 µl droplet of distilled water with a rate of 1 µl s^{-1} on the surface the CA is measured directly after reaching an equilibrium shape and after 30 s. The pristine samples are hydrophilic with a measured CA around 50° and all laser-machined surfaces reveal a hydrophobic characteristic with CA well above 120°. In contrary to the proposed behavior of a Wenzel state the laser ablation process modifies not only the topography, but also the surface-near chemistry. This may be attributed to the manufacturing in ambient condition evidenced by an observed slight color change of the ceramics to yellow, which is a sign of defects and especially oxygen vacancies [58]. The anticipated origin of this color change will have an impact on the total chemical potential leading to a modified CA and subsequently, altered blood coagulation.

To assess the impact of USP laser ablation on surface chemistry in more detail, an XPS study is carried out on the surface structured samples. The XPS survey scan reveals the elements as expected and the quantitative analysis is given with Table 2. With a first inspection at the surface showing no clear trend between the pristine and laser structured surfaces, depth profiling is carried out by Ar ion sputtering removing square fields of 4 mm^2. The depth is calibrated by removing 100 nm of Ta_2O_5 deposited on pure tantalum, within a total sputter time of 13.5 min. This allows to estimate the sputter rate to 7.39 nm min^{-1}. Fig. 10 presents the attained depth profiles for TZP and ATZ accordingly for the main constituents and carbon surface contamination. Additionally, the laser-patterned TZP sample with nano-roughness reveals 1.19 atomic percent concentration of Cu impurities attributed to the laser
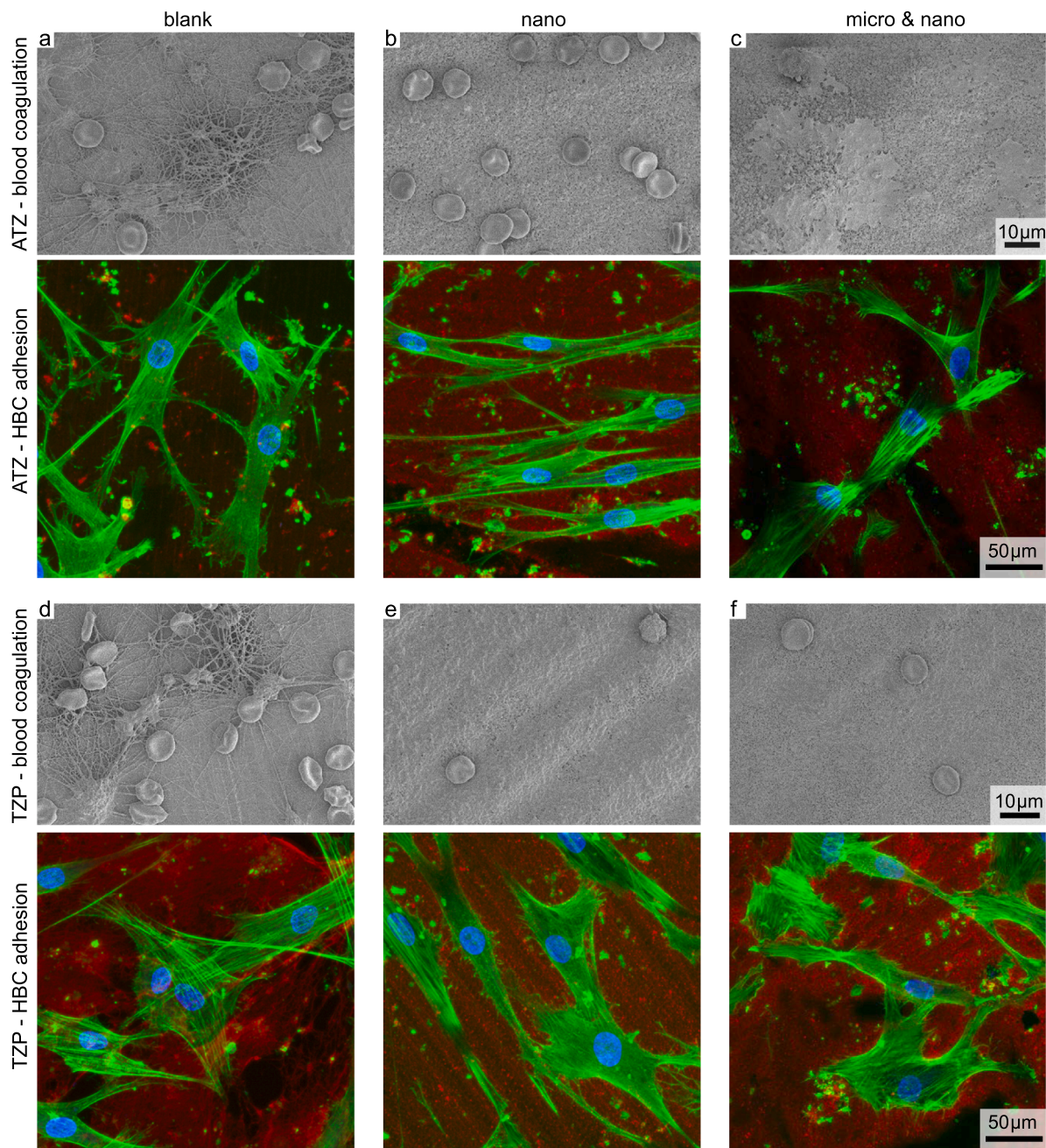
Fig. 8. Evaluation of the ATZ (a-c) and TZP (d-f) laser-structured surfaces for blood coagulation by SEM (upper graphs) and HBC adhesion by CLSM (bottom graphs). The adhered blood platelets and evolving fibrin network after 13–15 min shows the impact of laser structuring the ceramic surfaces on blood coagulation. Staining for cell nuclei (blue) and the actin cytoskeleton (green) demonstrates cell attachment and spreading on blood pre-incubated surfaces. Fibrinogen adsorption and formed fibrin network is shown in red. Representative images from n = 2 (SEM) and n = 3 (CLSM) independent experiments are shown. (For interpretation of the references to color in this figure legend, the reader is referred to the web version of this article.)

manufacturing, where the experimental testbed is used for different materials. A contamination during storage is unlikely, considering that the same conditions were used for all samples. Clearly, the carbon content due to storage or processing in ambient conditions decreases after the first removed layer for both ceramics being mainly existent on the surface. ZrO_2 is partially reduced upon Ar sputtering [59] resulting in a decreased O/Zr ratio. The small yttrium fraction stays constant after the first removed layer showing no sign of degradation and hafnium shows no apparent features. In contrast, the sputter depth profile of the ATZ ceramic reveals a decrease in oxygen and aluminum accompanied by an increase in zirconium. Comparing the two laser structured surfaces with the blank surface, an aluminum depletion evolves observable with

the increase in atomic concentration up to the maximal layer depth studied. Equivalent to TZP, the carbon concentration decreases and only covers the surface in a thin layer. Nevertheless, no detailed explanation of the change in wettability and associated bio-response can be stated with the attained data. One effect concerning the aluminum depletion could be correlated with the observed ablation characteristics of the ATZ ceramic. The sharp onset of the material removal ablates clusters of material and the alumina particle density seems to decrease after ablation. However, for a sound interpretation cross-sections inspected by high-resolution SEM or using transmission electron microscopy should be attained. Hence, the small trends in the depth profiling do not allow a consistent reasoning, but more detailed studies using surface-near
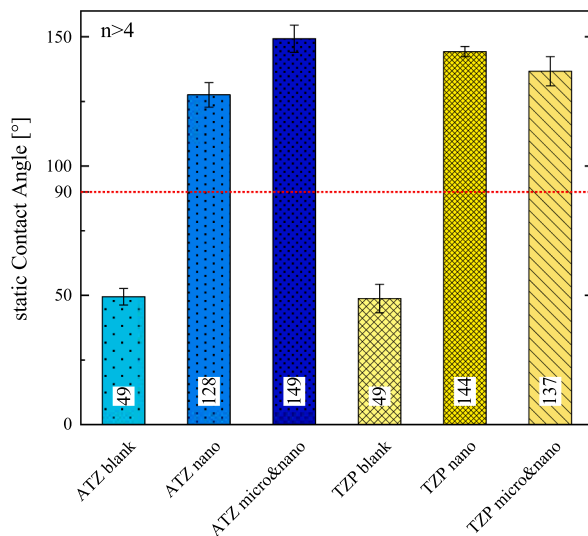
Fig. 9. Static contact angle of two samples per surface at more than two locations. For both ceramics laser machining induces a transition from hydrophilic to -phobic wettability.

Table 2
Atomic percent concentration of the different constituents from XPS measurement for the TZP and ATZ ceramic, respectively. For each surface from the blank, nano-roughness, and micro&nano an XPS determination is carried out.

Sample	C 1s	O 1s	Na 1s	Al 2p	Si 2p	Y 3d	Zr 3d	Hf 4f
ATZ blank	66.3	24.0	0.9	3.1	1	0.2	4.4	0.1
ATZ nano	50.5	34.8	0.7	3.0	0.4	0.6	9.7	0.1
ATZ micro&nano	54.7	32.4	0.6	2.6	0	0.6	8.7	0.1
TZP blank	65.4	23.9	–	–	–	0.6	9.8	0.0
TZP nano	43.8	37.7	–	–	–	0.9	15.8	0.1
TZP micro&nano	50.9	31.9	–	–	–	1.1	15.2	0.1

techniques like photo-luminescence would allow measuring band gap variations induced by defects and oxygen vacancies in more detail.

4. Conclusions and outlook

Laser machining with USP has proven to be a viable approach for rapid prototyping minimizing the total time for geometrical changes on hard-to-machine materials such as ceramics. A distinct parameter study and choice of strategies enabled a straight-forward patterning of complex 3D surface geometries with custom-tailored structures. Rationally designed topographies with hierarchical features have been introduced to ATZ and TZP ceramics and following an in depth material characterisation, the blood- as well as cell-material interaction was studied in vitro. The studied USP laser processes using orthogonal incidence condition unraveled a negligible impact on the materials phases assessed by electron microscopy, Raman mapping and XPS profiling. A detailed investigation of the surface using XPS showed a slight change in atomic oxygen concentration and depth profiling points to an aluminum depletion in the surface near region of the ATZ accompanied by an increasing zirconium portion. In contrast, the TZP only showed a slight decrease in zirconium, where both ceramics are covered by about 1 nm carbon. The introduced change in chemical potential altering the static contact angle to hydrophobic interferes with blood coagulation, but has no effect on cell attachment and spreading. Further studies employing the laser patterning in defined ambient conditions of vacuum and inert gas would allow to decouple the impact of induced chemistry change and topography on the bio-response, whereas long-term studies on cell
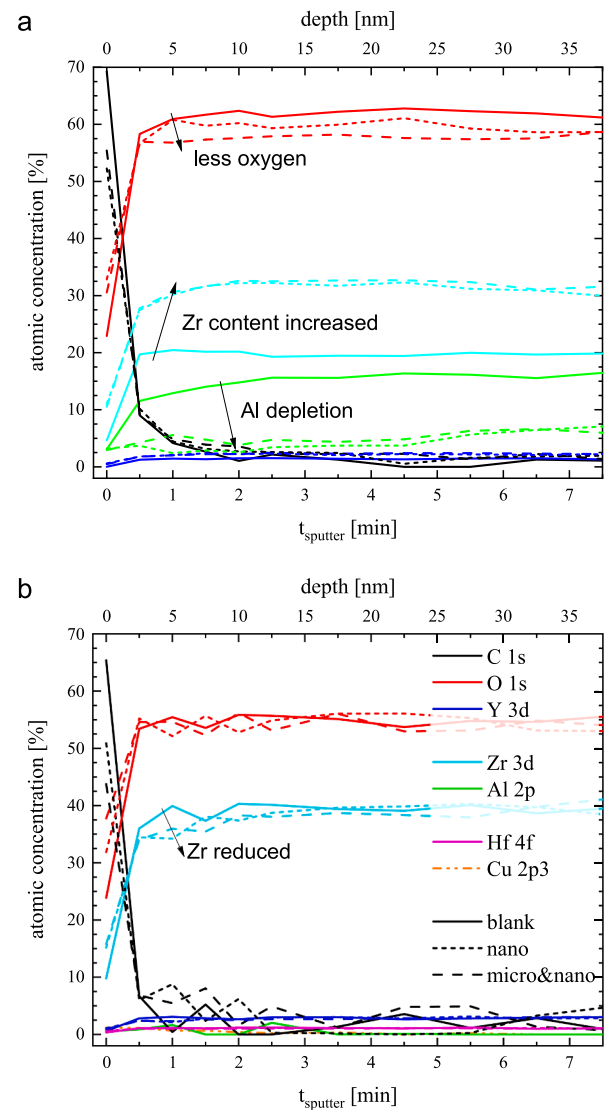

Fig. 10. XPS depth profiles following the main constituents of the ATZ (a) and TZP (b) specimen revealing a clear change in chemistry for ATZ correlated with the laser machining for the nano surface structures. For TZP Zr is reduced within the first 10 nm.

proliferation and differentiation as well as animal studies would allow to assess the tissue integration potential of the presented surfaces. Overall, the introduced routines reveal a high potential using a fast structuring route for surface development altering the blood- and tissue-material interaction to potentially enhance tissue integration of implants after surgery.

CRediT authorship contribution statement

Norbert Ackerl: Conceptualization, Data curation, Formal analysis, Funding acquisition, Investigation, Methodology, Project administration, Resources, Visualization, Writing - original draft, Writing - review & editing. **Alexander Hansen Bork:** Resources, Data curation, Formal analysis, Writing - review & editing. **Roland Hauert:** Formal analysis, Investigation, Resources, Writing - review & editing. **Eike Müller:** Conceptualization, Data curation, Formal analysis. **Markus Rottmar:** Conceptualization, Methodology, Project administration, Resources, Supervision, Writing - review & editing.

Declaration of Competing Interest

The authors declare that they have no known competing financial interests or personal relationships that could have appeared to influence the work reported in this paper.

Acknowledgments

References

[1] M. Navarro, A. Michiardi, O. Castaño, J.A. Planell, Biomaterials in orthopaedics, J. R. Soc. Interface 5 (27) (2008) 1137–1158, https://doi.org/10.1098/rsif.2008.0151.

[2] B. Stevens, Y. Yang, A. Mohandas, B. Stucker, K.T. Nguyen, A review of materials, fabrication methods, and strategies used to enhance bone regeneration in engineered bone tissues, J. Biomed. Mater. Res. - Part B Appl. Biomater. 85 (2) (2008) 573–582, https://doi.org/10.1002/jbm.b.30962.

[3] M. Geetha, A.K. Singh, R. Asokamani, A.K. Gogia, Ti based biomaterials, the ultimate choice for orthopaedic implants - a review, Prog. Mater. Sci. 54 (3) (2009) 397–425, https://doi.org/10.1016/j.pmatsci.2008.06.004.

[4] R. Osman, M. Swain, A critical review of dental implant materials with an emphasis on titanium versus zirconia, Materials (Basel) 8 (3) (2015) 932–958, https://doi.org/10.3390/ma8030932.

[5] D.A. Puleo, A. Nanci, Understanding and controlling the bone-implant interface, Biomaterials 20 (23–24) (1999) 2311–2321, https://doi.org/10.1016/S0142-9612(99)00160-X.

[6] V. Moraschini, L.A.C. Poubel, V.F. Ferreira, E.D.S. Barboza, Evaluation of survival and success rates of dental implants reported in longitudinal studies with a follow-up period of at least 10 years: A systematic review, Int. J. Oral Maxillofac. Surg. 44 (3) (2015) 377–388, https://doi.org/10.1016/j.ijom.2014.10.023.

[7] G. Wu, P. Li, H. Feng, X. Zhang, P.K. Chu, Engineering and functionalization of biomaterials via surface modification, J. Mater. Chem. B 3 (10) (2015) 2024–2042, https://doi.org/10.1039/C4TB01934B.

[8] L. Le Guéhennec, A. Soueidan, P. Layrolle, Y. Amouriq, Surface treatments of titanium dental implants for rapid osseointegration, Dent. Mater. 23 (7) (2007) 844–854, https://doi.org/10.1016/j.dental.2006.06.025.

[9] F. Rupp, L. Liang, J. Geis-Gerstorfer, L. Scheideler, F. Hüttig, Surface characteristics of dental implants: A review, Dent. Mater. 34 (1) (2018) 40–57, https://doi.org/10.1016/j.dental.2017.09.007.

[10] J.Y. Martin, Z. Schwartz, T.W. Hummert, D.M. Schraub, J. Simpson, J. Lankford, D. D. Dean, D.L. Cochran, B.D. Boyan, Effect of titanium surface roughness on proliferation, differentiation, and protein synthesis of human osteoblast-like cells (mg63), J. Biomed. Mater. Res. 29 (3) (1995) 389–401, https://doi.org/10.1002/jbm.820290314.

[11] E. Rompen, O. Domken, M. Degidi, A.E.P. Pontes, A. Piattelli, The effect of material characteristics, of surface topography and of implant components and connections on soft tissue integration: A literature review, Clin. Oral Implants Res. 17 (2) (2006) 55–67, https://doi.org/10.1111/j.1600-0501.2006.01367.x.

[12] M. Rottmar, E. Müller, S. Guimond-Lischer, M. Stephan, S. Berner, K. Maniura-Weber, Assessing the osteogenic potential of zirconia and titanium surfaces with an advanced in vitro model, Dent. Mater. 35 (1) (2019) 74–86, https://doi.org/10.1016/j.dental.2018.10.008.

[13] R.G. Flemming, C.J. Murphy, G.a. Abrams, S.L. Goodman, P.F. Nealey, Effects of synthetic micro- and nano-structured surfaces on cell behavior, Biomaterials 20 (1999) 573–588, https://doi.org/10.1016/S0142-9612(98)00209-9.

[14] P. Vandrangi, S.C. Gott, R. Kozaka, V.G.J. Rodgers, M.P. Rao, Comparative endothelial cell response on topographically patterned titanium and silicon substrates with micrometer to sub-micrometer feature sizes, PLoS One 9 (10) (2014) e111465, https://doi.org/10.1371/journal.pone.0111465.

[15] M. Bereznai, I. Pelsöczi, Z. Tóth, K. Turzó, M. Radnai, Z. Bor, a. Fazekas, Surface modifications induced by ns and sub-ps excimer laser pulses on titanium implant material, Biomaterials 24 (23) (2003) 4197–4203, https://doi.org/10.1016/S0142-9612(03)00318-1.

[16] J.P. Ulerich, L.C. Ionescu, J. Chen, W.O. Soboyejo, C.B. Arnold, Modifications of Ti-6Al-4V surfaces by direct-write laser machining of linear grooves, Proc. SPIE 6458 (2007), https://doi.org/10.1117/12.713964, 645819-645819-10.

[17] A.Y. Vorobyev, C. Guo, Femtosecond laser structuring of titanium implants, Appl. Surf. Sci. 253 (17) (2007) 7272–7280, https://doi.org/10.1016/j.apsusc.2007.03.006.

[18] A. Kuczyńska-Zemła, E. Kijeńska-Gawrońska, M. Pisarek, P. Borowicz, W. Swieszkowski, H. Garbacz, Effect of laser functionalization of titanium on bioactivity and biological response, Appl. Surf. Sci. 525 (2019), https://doi.org/10.1016/j.apsusc.2020.146492.

[19] C.A. Shapoff, B. Lahey, P.A. Wasserlauf, D.M. Kim, Radiographic analysis of crestal bone levels around laser-lok collar dental implants, Int. J. Periodontics Restorative Dent. 30 (2) (2010) 129–137, https://doi.org/10.11607/prd.00.0911.

[20] M. Nevins, M. Nevins, L. Gobbato, H.-J. Lee, C.-W. Wang, D.M. Kim, Maintaining Interimplant Crestal Bone Height Via a Combined Platform- Switched, Laser-Lok Implant/Abutment System: A Proof-of-Principle Canine Study, Int. J. Periodontics Restor. Dent. 33 (3) (2013) 261–267, https://doi.org/10.11607/prd.1773.

[21] M. Martínez-Calderon, R.J. Martín-Palma, A. Rodríguez, M. Gómez-Aranzadi, J. P. García-Ruiz, S.M. Olaizola, M. Manso-Silván, Biomimetic hierarchical micro/nano texturing of TiAlV alloys by femtosecond laser processing for the control of cell adhesion and migration, Phys. Rev. Mater. 4 (5) (2020) 1–10, https://doi.org/10.1103/physrevmaterials.4.056008.

[22] J. Chevalier, What future for zirconia as a biomaterial? Biomaterials 27 (4) (2006) 535–543, https://doi.org/10.1016/j.biomaterials.2005.07.034.

[23] Y. Chang, R. Bermejo, O. Ševeček, G.L. Messing, Design of alumina-zirconia composites with spatially tailored strength and toughness, J. Eur. Ceram. Soc. 35 (2) (2015) 631–640, https://doi.org/10.1016/j.jeurceramsoc.2014.09.017.

[24] M.N. Abdallah, Z. Badran, O. Ciobanu, N. Hamdan, F. Tamimi, Strategies for Optimizing the Soft Tissue Seal around Osseointegrated Implants, Adv. Healthc. Mater. 6 (20) (2017) 1–24, https://doi.org/10.1002/adhm.201700549.

[25] F. Kern, H. Reveron, J. Chevalier, R. Gadow, Mechanical behaviour of extremely tough tzp bioceramics, J. Mech. Behav. Biomed. Mater. 90 (2019) 395–403, https://doi.org/10.1016/j.jmbbm.2018.11.001.

[26] P. Kohorst, L. Borchers, J. Strempel, M. Stiesch, T. Hassel, F.-W. Bach, C. Hübsch, Low-temperature degradation of different zirconia ceramics for dental applications, Acta Biomater. 8 (3) (2012) 1213–1220, https://doi.org/10.1016/j.actbio.2011.11.016.

[27] G. Magnani, A. Brillante, Effect of the composition and sintering process on mechanical properties and residual stresses in zirconia -alumina composites, J. Eur. Ceram. Soc. 25 (15) (2005) 3383–3392, https://doi.org/10.1016/j.jeurceramsoc.2004.09.025.

[28] X.H. Zhang, Z.X. Kang, S. Li, Q.P. Wu, Z.C. Zhang, Experimental investigations on the impact of different laser macro-structured diamond grinding wheels on alumina ceramic, Int. J. Adv. Manuf. Technol. 96 (5–8) (2018) 1959–1969, https://doi.org/10.1007/s00170-018-1644-3.

[29] N. Ackerl, P. Boerner, K. Wegener, Toward application of hierarchical structures by ultrashort pulsed laser ablation, J. Laser Appl. 31 (2) (2019) 022501, https://doi.org/10.2351/1.5096079.

[30] C. Stamatopoulos, A. Milionis, N. Ackerl, M. Donati, P. Leudet de la Vallée, P. Von Rohr, D. Poulikakos, Droplet self-propulsion on superhydrophobic microtracks, ACS Nano 14 (10) (2020) 12895–12904, https://doi.org/10.1021/acsnano.0c03849.

[31] J. Bonse, R. Koter, M. Hartelt, D. Spaltmann, S. Pentzien, S. Höhm, A. Rosenfeld, J. Krüger, Tribological performance of femtosecond laser-induced periodic surface structures on titanium and a high toughness bearing steel, Appl. Surf. Sci. 336 (2015) 21–27, https://doi.org/10.1016/j.apsusc.2014.08.111.

[32] F.L.P. Veenstra, N. Ackerl, A.J. Martín, J. Pérez-Ramírez, Laser-Microstructured Copper Reveals Selectivity Patterns in the Electrocatalytic Reduction of CO_2, Chem 6 (7). doi: 10.1016/j.chempr.2020.04.001.

[33] N. Ackerl, M. Warhanek, J. Gysel, K. Wegener, Ultrashort-pulsed laser machining of dental ceramic implants, J. Eur. Ceram. Soc. 39 (4) (2019) 1635–1641, https://doi.org/10.1016/j.jeurceramsoc.2018.11.007.

[34] Y. Di Maio, J.P. Colombier, P. Cazottes, E. Audouard, Ultrafast laser ablation characteristics of pzt ceramic: Analysis methods and comparison with metals, Opt. Lasers Eng. 50 (11) (2012) 1582–1591, https://doi.org/10.1016/j.optlaseng.2012.05.022.

[35] A. Narazaki, H. Takada, D. Yoshitomi, K. Torizuka, Y. Kobayashi, Study on nonthermal–thermal processing boundary in drilling of ceramics using ultrashort pulse laser system with variable parameters over a wide range, Appl. Phys. A Mater. Sci. Process. 126 (4) (2020) 1–8, https://doi.org/10.1007/s00339-020-3410-2.

[36] A.N. Samant, N.B. Dahotre, Laser machining of structural ceramics - a review, J. Eur. Ceram. Soc. 29 (6) (2009) 969–993, https://doi.org/10.1016/j.jeurceramsoc.2008.11.010.

[37] H. Wang, H. Lin, C. Wang, L. Zheng, X. Hu, Laser drilling of structural ceramics - a review, J. Eur. Ceram. Soc. 37 (4) (2017) 1157–1173, https://doi.org/10.1016/j.jeurceramsoc.2016.10.031.

[38] L. Gremillard, L. Cardenas, H. Reveron, T. Douillard, A. Vogl, K. Hans, T. Oberbach, Microstructure and hydrothermal ageing of alumina-zirconia composites modified by laser engraving, J. Eur. Ceram. Soc. 40 (5) (2020) 2077–2089, https://doi.org/10.1016/j.jeurceramsoc.2020.01.027.

[39] N. Ackerl, J. Gysel, M.G. Warhanek, K. Wegener, Ultra-short pulsed laser manufacturing of yttria stabilized alumina-toughened zirconia dental implants, in: P. Rechmann, D. Fried (Eds.), Lasers Dent. XXV, vol. 10857, SPIE, 2019, pp. 108570J1-10. doi:10.1117/12.2507495.

[40] A. Daskalova, L. Angelova, A. Carvalho, A. Trifonov, C. Nathala, F. Monteiro, I. Buchvarov, Effect of surface modification by femtosecond laser on zirconia based ceramics for screening of cell-surface interaction, Appl. Surf. Sci. 513 (January). doi: 10.1016/j.apsusc.2020.145914.

[41] F. Zandiehnadem, R. Murray, W. Ching, Electronic structures of three phases of zirconium oxide, Phys. B+C 150 (1–2) (1988) 19–24, https://doi.org/10.1016/0378-4363(88)90099-X.

[42] H. Jiang, R.I. Gomez-Abal, P. Rinke, M. Scheffler, Electronic band structure of zirconia and hafnia polymorphs from the gw perspective, Phys. Rev. B - Condens. Matter Mater. Phys. 81 (8) (2010) 1–9, https://doi.org/10.1103/PhysRevB.81.085119.

[43] S. Ciraci, I.P. Batra, Electronic structure of α- alumina and its defect states, Phys. Rev. B 28 (2) (1983) 982–992, https://doi.org/10.1103/PhysRevB.28.982.

[44] S.-D. Mo, Y.-N. Xu, W.-Y. Ching, Electronic and structural properties of bulk γ-Al2O3, J. Am. Ceram. Soc. 80 (5) (2005) 1193–1197, https://doi.org/10.1111/j.1151-2916.1997.tb02963.x.

[45] N. Ackerl, M. Warhanek, J. Gysel, K. Wegener, Path calculation of 7-axes synchronous quasi-tangential laser manufacturing, Int. J. Adv. Manuf. Technol. 103 (1–4) (2019) 1105–1116, https://doi.org/10.1007/s00170-019-03540-5.

[46] B. Neuenschwander, G.F. Bucher, C. Nussbaum, B. Joss, M. Muralt, U.W. Hunziker, P. Schuetz, Processing of metals and dielectric materials with ps-laserpulses: results, strategies, limitations and needs, in: H. Niino, M. Meunier, B. Gu, G. Hennig (Eds.), Laser Appl. Microelectron. Optoelectron. Manuf. XV, vol. 7584, SPIE, 2010, pp. 75840R1-14. doi: 10.1117/12.846521.

[47] C.S. Nathala, A. Ajami, W. Husinsky, B. Farooq, S.I. Kudryashov, A. Daskalova, I. Bliznakova, A. Assion, Ultrashort laser pulse ablation of copper, silicon and gelatin: effect of the pulse duration on the ablation thresholds and the incubation coefficients, Appl. Phys. A Mater. Sci. Process. 122 (2) (2016) 1–8, https://doi.org/10.1007/s00339-016-9625-6.

[48] C. Gaudiuso, G. Giannuzzi, A. Volpe, P.M. Lugarà, I. Choquet, A. Ancona, Incubation during laser ablation with bursts of femtosecond pulses with picosecond delays, Opt. Express 26 (4) (2018) 3801, https://doi.org/10.1364/OE.26.003801.

[49] B. Neuenschwander, B. Jäggi, M. Schmid, G. Hennig, Surface structuring with ultra-short laser pulses: Basics, limitations and needs for high throughput, Phys. Procedia 56 (2014) 1047–1058, https://doi.org/10.1016/j.phpro.2014.08.017.

[50] M. Gaidys, A. Žemaitis, P. Gečys, M. Gedvilas, Efficient picosecond laser ablation of copper cylinders, Appl. Surf. Sci. 483 (2019) 962–966, https://doi.org/10.1016/j.apsusc.2019.04.002.

[51] N. Ackerl, K. Wegener, Ablation characteristics of alumina and zirconia ceramics on ultra-short pulsed laser machining, J. Laser Micro/Nanoengineering 14 (2). doi: 10.2961/jlmn.2019.02.0009.

[52] P. Boerner, M. Hajri, N. Ackerl, K. Wegener, Experimental and theoretical investigation of ultrashort pulsed laser ablation of diamond, J. Laser Appl. 31 (2) (2019) 022202, https://doi.org/10.2351/1.5096088.

[53] E. Roitero, F. Lasserre, M. Anglada, F. Mücklich, E. Jiménez-Piqué, A parametric study of laser interference surface patterning of dental zirconia: Effects of laser parameters on topography and surface quality, Dent. Mater. 33 (1) (2017) e28–e38, https://doi.org/10.1016/j.dental.2016.09.040.

[54] X. Zhu, J. Chen, L. Scheideler, R. Reichl, J. Geis-Gerstorfer, Effects of topography and composition of titanium surface oxides on osteoblast responses, Biomaterials 25 (18) (2004) 4087–4103, https://doi.org/10.1016/j.biomaterials.2003.11.011.

[55] G. Zhao, A.L. Raines, M. Wieland, Z. Schwartz, B.D. Boyan, Requirement for both micron- and submicron scale structure for synergistic responses of osteoblasts to substrate surface energy and topography, Biomaterials 28 (18) (2007) 2821–2829, https://doi.org/10.1016/j.biomaterials.2007.02.024.

[56] X. Zhao, D. Vanderbilt, Phonons and lattice dielectric properties of zirconia, Phys. Rev. B - Condens. Matter Mater. Phys. 65 (7) (2002) 1–10, https://doi.org/10.1103/PhysRevB.65.075105.

[57] B.S. Kopf, S. Ruch, S. Berner, N.D. Spencer, K. Maniura-Weber, The role of nanostructures and hydrophilicity in osseointegration: In-vitro protein-adsorption and blood-interaction studies, J. Biomed. Mater. Res. Part A 103 (8) (2015) 2661–2672, https://doi.org/10.1002/jbm.a.35401.

[58] Y. Kodera, C. Hardin, J. Garay, Transmitting, emitting and controlling light: Processing of transparent ceramics using current-activated pressure-assisted densification, Scr. Mater. 69 (2) (2013) 149–154, https://doi.org/10.1016/j.scriptamat.2013.02.013.

[59] J. Greene, R. Klinger, T. Barr, L. Welsh, Auger and X-ray photoelectron spectroscopy studies of preferential sputtering in Y2O3-doped ZrO2 films, Chem. Phys. Lett. 62 (1) (1979) 46–50, https://doi.org/10.1016/0009-2614(79)80410-8.